Journal of
Materials Chemistry A

Materials for energy and sustainability

Accepted Manuscript

This article can be cited before page numbers have been issued, to do this please use: S. Chen, Y. Li, Z. Bu, F. Yang, J. Luo, Q. An, Z. Zeng, J. Wang and S. Deng, *J. Mater. Chem. A*, 2020, DOI: 10.1039/D0TA08496D.

ROYAL SOCIETY OF CHEMISTRY

rsc.li/materials-a

View Article Online
DOI: 10.1039/D0TA08496D

Boosting CO_2-to-CO Conversion on a Robust Single-Atom Copper Decorated Carbon Catalyst by Enhancing Intermediate Binding Strength

Shixia Chen, [a‡] Yuewei Li, [a‡] Zhuogang Bu, [a] Fangqi Yang, [a] Junhui Luo, [a] Qizheng An, [b] Zheling Zeng [a], Jun Wang, *[a] and Shuguang Deng *[c]

[a]School of Resources Environmental & Chemical Engineering, Nanchang University, Nanchang, 330031, China

[b]School of Material Science and Engineering and Institute for Advanced Study, Nanchang University, Nanchang, 330031 P. R. China

[c]School for Engineering of Matter, Transport and Energy, Arizona State University, 551 E. Tyler Mall, Tempe, AZ 85287, USA

[‡] These authors contributed equally to this work.

*Corresponding authors:

1. E-mail: shuguang.deng@asu.edu (S. Deng)

2. E-mail: jwang7@ncu.edu.cn (J. Wang)

View Article Online
DOI: 10.1039/D0TA08496D

Abstract: The ability to manipulate the binding strengths of intermediates on a catalyst is extremely challenging but essential for active and selective CO_2 electroreduction (CO_2RR). Single-atom copper anchored on nitrogenated carbon (Cu-N-C) structure is still rarely unexplored for efficient CO production. Herein, we demonstrate a plausible hydrogen-bonding promoted strategy that significantly enhances the *COOH adsorption and facilitates the *CO desorption on a Cu-N-C catalyst. The as-prepared Cu-N-C catalyst with Cu-N_3 coordination achieves a high CO Faradaic efficiency (FE) of 98% at -0.67 V (vs reversible hydrogen electrode) as well as superior stability (FE sustains above 90% over 20 h). Notably, in the three-phase flow cell configuration, a remarkable CO_2 to CO FE of 99% at -0.67 V accompanying a large CO partial current density of 131.1 mA cm^{-2} at -1.17 V was observed. Density functional theory calculations reveal that the Cu-N_3 coordination is potentially stabilized by an extended carbon plane with six nitrogen vacancies, while, three unoccupied N sites are spontaneously saturated by protons during CO_2RR. Therefore, the hydrogen-bonds formed between the adsorbed *COOH and adjacent protons significantly reduce the energy barrier of *COOH formation. After the first proton-coupled electron transfer process, the adsorbed *CO species are easily released to boost the CO production.

Keywords: CO_2 electroreduction; single Cu atoms; CO production; binding strength; flow cell

View Article Online
DOI: 10.1039/D0TA08496D

Introduction

The ever-growing carbon dioxide (CO_2) level caused by the excessive use of fossil fuels has led to serious environmental problems.[1,2] On the other hand, CO_2 is a non-toxic, inexpensive, and abundant C1 resource for the production of various chemicals.[3] The electrochemical reduction of carbon dioxide (CO_2RR) has been considered as a green, facile, and economical strategy to produce high-value two-electron reduction product carbon monoxide (CO) due to the superior selectivity and yield compared with those of other CO_2 reduction pathways.[4] Thus, efficient CO_2-to-CO conversions catalysts with excellent activity and stability are highly desired, which is a promising route to reduce CO_2 emissions and achieve a carbon-neutral cycle.[5,6]

Manipulating the binding strength of intermediates on catalysts is of great importance to design highly active and selective CO_2RR electrocatalysts for CO_2 to CO conversion, especially for emerging single metal ions coordinated N-doped carbon (M-N-C) materials.[7-12] Among the reported M-N-C catalysts, Fe-N-C could only maintain high CO FEs (above 90%) within a narrow operation potential window of 0.2 V (all potentials are indicated vs. RHE afterward) due to the strong *CO adsorption on Fe-N sites.[13-15] Ni-N-C exhibited high CO FEs at relatively high operation potentials (-0.6 ~ -1.2 V) owing to the weak binding strength of *COOH on the Ni-N sites.[16-18] In contrast, Cu-N-C catalysts have rarely been reported for efficient CO production, instead, they tend to produce deeply reduced products. As exemplified by the typical Cu-N_4 structures, the methanol production with a FE of 44% at -0.9 V and ethanol production

View Article Online
DOI: 10.1039/D0TA08496D

with a FE of 55% at -1.2 V have been reported.[19,20] Note that instead of spontaneous desorption of the *CO species, a positive free-energy barrier (0.12 V) of *CO desorption on CuN_4 coordination was observed.[19] Thus they prefer to be further reduced at relatively high overpotentials. Very recently, our group reported the atomically dispersed Cu-N_4 moieties for effect CO production with a FE of 92% at -0.7 V.[21] Nevertheless, the efficient CO_2-to-CO conversion on a Cu-N-C electrocatalyst in aqueous solutions is still largely unexplored so far.

Herein, we demonstrate a hydrogen-bond promoted strategy to manipulate the binding strengths of intermediates to achieve an efficient CO_2-to-CO conversion on Cu-N-C. The high active atomic interface enables a high CO FE of 98% at a relatively low overpotential of -0.67 V with long-term stability over 20 h continuous electroreduction process. Meanwhile, by applying Cu-N-C catalyst in a three-phase flow cell, a remarkable CO FE of 99% was realized at -0.67 V with a large CO partial current density of 131.3 mA cm^{-2} at -1.17 V. Density functional theory (DFT) calculations reveal that the single Cu atoms are stabilized by a unique proton-saturated Cu-N_6 coordination with three proton-saturated N sites and one Cu-N_3 coordination. Notably, the hydrogen-bond formed between the O atom of *COOH and the H atom of adjacent H-saturated N site significantly reduces the energy barrier of *COOH formation. Meanwhile, the *CO species are easily released to boost the CO production after the first proton-coupled electron transfer process. This work provides new insights into the mechanism of CO_2-to-CO conversion on a Cu-N-C structure at the atomic level.

Results and Discussion

View Article Online
DOI: 10.1039/D0TA08496D

Fabrication and characterization of Cu-N-C catalyst

The schematic fabrication procedures of the Cu-N-C catalyst are illustrated in Figure 1a and the detailed synthesis methods are provided in the *Supporting Information*. Briefly, Cu and Zn co-doped ZIF-8 (Cu/Zn-ZIF-8) with a Cu/Zn molar ratio of 1:8 is prepared *via* a hydrothermal method. After calcination at 1000 ℃ in the Ar atmosphere, the evaporation of Zn species at 907 ℃ creates abundant micropores and Cu atoms are stabilized by N coordination instead of agglomeration. For comparison, nitrogen-doped carbon (N-C) without Cu doping was prepared from pristine ZIF-8 in the same way. The scanning electron microscopy (SEM) images of Cu/Zn-ZIF-8 and ZIF-8 showed the regular dodecahedron morphology with a uniform size of 2~4 μm (Figure S1). After carbonization, the dodecahedron morphology could be retained on Cu-N-C and N-C with a slightly reduced particle size (Figures 1b and S2). Transmission electron microscopy (TEM) and high-resolution TEM (HR-TEM) showed that no Cu nanoparticles or clusters were observed on Cu-N-C (Figures 1c and 1d). The corresponding selected area electron diffraction (SAED) patterns showed a typical character of disordered carbon substrate (Figure 1c insert). The high-angle annular dark-field scanning transmission electron microscopy (HAADF-STEM) with a spherical aberration corrector was applied to identify the single Cu atoms. As shown in Figures 1e and 1f, the bright dots that are encased in yellow dashed circles are recognized as the isolated and well-dispersed Cu atoms. The HR-TEM and HAADF-STEM images from different regions confirm the homogeneous distribution of isolated Cu atoms (Figure S3). Besides, energy-dispersive X-ray spectroscopy (EDS) mappings

View Article Online
DOI: 10.1039/D0TA08496D

(Figure 1g) revealed the homogeneous distributions of Cu and N elements throughout the carbon matrix. The carbon matrix primarily provides the substance to well disperse the Cu atoms to create single Cu active sites, meanwhile, the high conductivity and large surface area will facilitate the electron transport and boost the mass transfer during the electrocatalytic process. The Cu content on Cu-N-C was determined to be 0.61 wt.% by inductively coupled plasma mass spectrometer (ICP-MS).

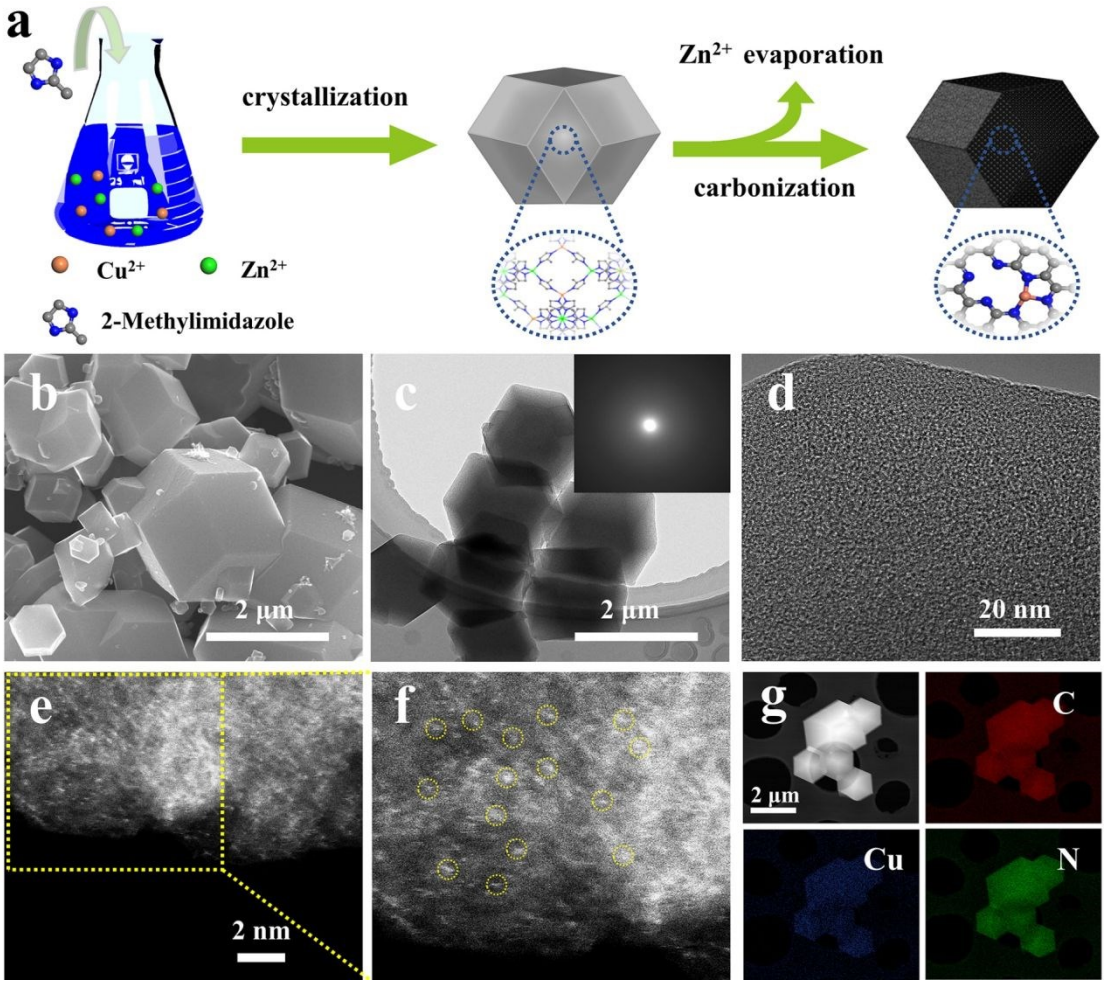

Figure 1. (a) Schematic illustration of Cu-N-C catalyst synthesis; (b) SEM, (c) TEM, (d) HR-TEM, and (e, f) HAADF-STEM images of Cu-N-C; (g) The corresponding EDS mappings of C, Cu, and N elements.

X-ray diffraction (XRD) patterns of Cu/Zn-ZIF-8 and ZIF-8 (Figure S4) matched

View Article Online
DOI: 10.1039/D0TA08496D

well with the simulated pattern, indicating that the impregnation of Cu will not change the topology of the ZIF-8 framework. In contrast, two broad diffraction peaks were observed in the XRD patterns of Cu-N-C and N-C (Figure S5), which could be assigned to the (002) and (100) planes of amorphous carbon planes, suggesting the complete transformation from ZIF-8 and Cu/Zn-ZIF-8 to N-C and Cu-N-C.[22] Meanwhile, the absence of Cu-based diffraction peaks coincides well with the HR-TEM and HAADF-STEM observations. Raman spectra exhibited two peaks correspond to the D (1350 cm^{-1}) and G bands (1580 cm^{-1}), which represents the vibration of sp^3 dangling and in-plane sp^2 carbons, respectively (Figure S6).[23] The chemical compositions of the obtained samples were investigated by X-ray photoelectron spectroscopy (XPS) as depicted in Figure S7, and the detailed C, N, and O contents are summarized in Table S2. The Cu content is measured to be 0.12 at.% and no other metal contaminants are observed. The XPS N1s spectra of Cu-N-C further confirmed the considerable presence of M-N-C moieties (Figure 2a). During the high-temperature annealing, the N-5 species in ZIF-8 will evolve to various N species due to the graphitization and oxidation processes.[7,8] The high-resolution N spectra of Cu-N-C and N-C could be deconvoluted into pyridinic N (398.5±0.1 eV), pyrrolic N (401.1±0.1 eV), and graphitic N (402.3±0.2 eV).[24-26] Notably, the emerging Cu-N peak located at 399.0±0.2 eV on Cu-N-C demonstrates the formed Cu-N coordination.[27] In Figure S7b, the high-resolution Cu $2p^{3/2}$ peak at 933.7 eV indicates the valence state of Cu is between 0 and +2 on Cu-N-C. [28]

The specific Brunauer-Emmett-Teller (BET) surface area of Cu-N-C and N-C catalysts were probed by the N_2 sorption isotherms at 77 K (Figure S8a). The steep N_2

View Article Online
DOI: 10.1039/D0TA08496D

adsorption at low-pressure range manifests their microporous nature. The BET specific surface area is calculated to be 845 and 858 m^2 g^{-1} for Cu-N-C and N-C, respectively. The pore size distributions are also very similar, with dominant pores centered at 0.78 and 0.77 nm on Cu-N-C and N-C, respectively (Figures S8b and S8c). The CO_2 adsorption capacity at 298 K was measured to be 3.48 and 3.37 mmol g^{-1} on Cu-N-C and N-C, respectively (Figure S9). The almost identical CO_2 capacities indicate that the isolated Cu atoms showed limited effects on the CO_2 adsorption affinity, which could further be verified by a similar CO_2 isosteric adsorption heat (Figure S9d). Therefore, the almost coincident morphology and CO_2 affinity could be excluded from differentiating the CO_2RR performances of Cu-N-C and N-C.

To investigate the coordination environment of Cu species at the atomic level, the Cu K-edge X-ray absorption near-edge structure (XANES) of Cu-N-C with the reference samples is illustrated in Figure 2b. The absorption edge of Cu-N-C located between Cu_2O and CuO, confirms that the oxidation valence state of the Cu atom is between Cu^{1+} and Cu^{2+}.[29] The coordination environment was demonstrated by the extended X-ray absorption fine structure (EXAFS) spectrum (Figure 2c), the Fourier transform (FT) k^3-weighted $\chi(k)$ EXAFS spectrum of Cu-N-C showed a main peak at 1.4 Å that is shorter than that of Cu phthalocyanine (CuPc, Cu-N_4, 1.65 Å). Notably, no Cu-Cu coordination peak was observed at 2.2 Å, which unambiguously implied the complete absence of Cu nanoparticles or clusters. Moreover, the EXAFS spectrum of Cu-N-C could be fitted and the coordination number of Cu was determined to be 3.2 (Figure 2d and Table S4). In addition, the wavelet transform (WT) plot of Cu-N-C

View Article Online
DOI: 10.1039/D0TA08496D

showed the maximum WT centered at 5.5 $Å^{-1}$ that is close to that of CuPc (Figures 2e and S10), confirming the existing Cu−N bond on Cu-N-C. In contrast, the highest WT plot position of Cu-Cu bond is at about 6~8 $Å^{-1}$.

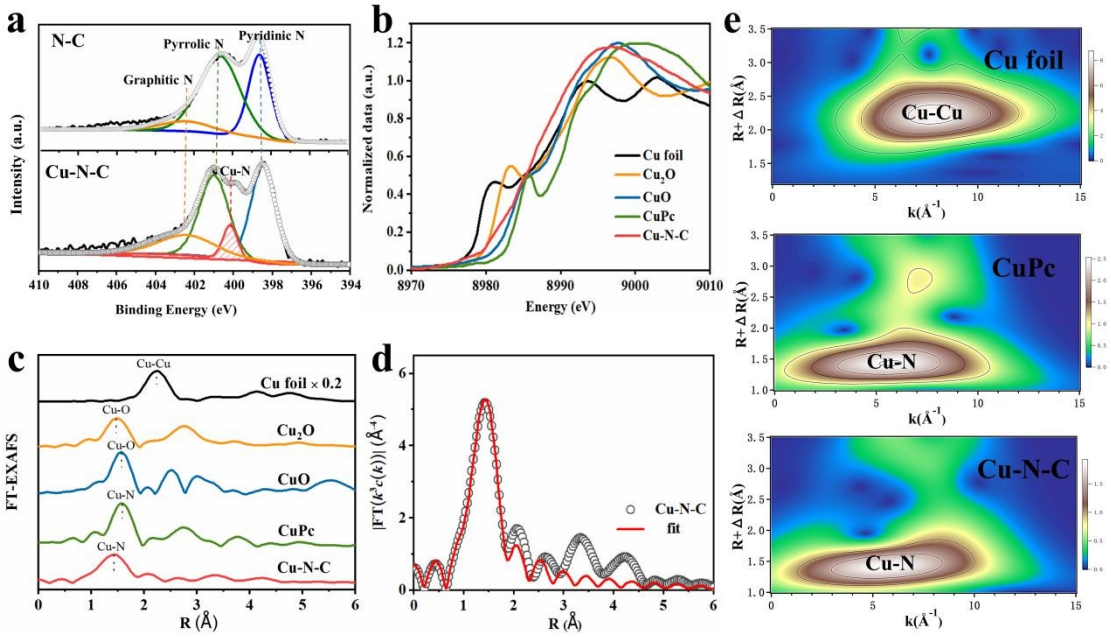

Figure 2. (a) XPS N1s signal of N-C and Cu-N-C; (b) the normalized XANES spectra at the Cu K-edge; (c) Fourier transformation of the EXAFS spectra at R space; (d) the EXAFS fitting for Cu-N-C; and (e) the wavelet transform (WT) plot.

CO_2 electroreduction performance

The CO_2 electroreduction activities of Cu-N-C, N-C, and CuPc were evaluated in a gas-tight H-type cell (Figure S11). As revealed by the linear sweep voltammetry (LSV) curves (Figure 3a), Cu-N-C exhibited a substantially larger cathodic current density compared with the N-C and CuPc in CO_2-saturated 0.5 M $KHCO_3$ solution (pH =7.2). Meanwhile, the recorded current density on Cu-N-C is considerably larger than that in Ar-saturated 0.5 M $KHCO_3$ solution (Figure S12a), confirming that the currents are

View Article Online
DOI: 10.1039/D0TA08496D

mainly devoted to the electrocatalytic CO_2 reduction. The potential-dependent CO_2RR evaluation is performed at the potential range of -0.37 to -0.97 V and the products were detected by gas chromatography (Figure S13) and ^1H nuclear magnetic resonance (NMR). CO and H_2 are the main gaseous products with trace amounts of C_2H_4 and C_2H_6 that only yield at high potential (Figures 3b and S14), and no liquid products were detected (Figure S15). The catalysts exhibit stable time-dependent total current densities at different applied potentials for 2000 s (Figure. S16). The CO current density (j_{CO}) of Cu-N-C reached 4.6 mA cm^{-2} at -0.77 V that outperformed that of N-C and CuPc (Figure S17a). Particularly, Cu-N-C achieved a maximum CO FE of 98% at -0.67 V; while N-C and CuPc could only achieve a CO FE of 28% and 22% at -0.67 V, respectively (Figure S17b), suggesting the dominating active sites of Cu-N-C. Meanwhile, it also outperforms many benchmark M-N-C catalysts, such as Ni-N_4 (97.8%),[30] Fe-N-C (87%),[11] Co-N_4 (82%),[31] and Fe-N_4 (94%).[32] Furthermore, an isotope labeling experiment using $^{13}CO_2$ as the feedstock confirms that the CO product originates from the reduction of CO_2 (Figure S18).

Tafel slopes were calculated to gain further insight into the electro-kinetics of CO_2RR. As shown in Figure 3c, the lowest Tafel slope of 156 mV dec^{-1} was observed on Cu-N-C followed by CuPc (239 mV dec^{-1}) and N-C (309 mV dec^{-1}), indicating its superior kinetics for the CO production. Moreover, electrochemical active surface areas (ECSA) were estimated by the double-layer capacitance (C_{dl}) measurements, which is obtained from the CV curves at different scan rates (Figure S19a-d). Cu-N-C exhibited a greater C_{dl} of 2.5 mF cm^{-2} that is 1.4 and 9.6 fold

View Article Online
DOI: 10.1039/D0TA08496D

larger than N-C and CuPc, respectively (Figure S19e). Since Cu-N-C and N-C displayed almost identical BET surface area, the larger ECSA can be attributed to the exposure of electroactive and accessible Cu sites. The electrochemical impedance spectroscopy (EIS) displays a smaller charge transfer resistance (R_{ct}) on Cu-N-C compared with N-C and CuPc, confirming the faster electron-transfer during the CO_2RR (Figure S19f). Furthermore, the intrinsic activity of Cu-N-C is further disclosed by the turnover frequency (TOF) calculation. The Cu-N-C also shows an outstanding CO TOF value of 922 hr^{-1} normalized to the Cu site at −0.77 V (Figure S20). It is worth noting that the high CO FE and TOF are simultaneously achieved on Cu-N-C (Figure 3d).[11,31,33-37] Meanwhile, Cu-N-C also exhibits a steady current density for CO production with a nearly undeclined FE during the consecutive CO_2RR over 20 h, indicating its long-term stability (Figure 3e). The morphology was well maintained and no Cu particles/clusters were observed in the post-cycling TEM and HR-TEM images. And the absence of Cu agglomeration or cluster was also confirmed by the XRD patterns. Undetectable Cu species, in the electrolyte after cycling tests, was verified by the ICP with a detection limit of ~100 ppb. These analyses suggesting the prepared Cu-N-C catalyst is robust and stable (Figure S22). Flow cell configuration was further assembled to evaluate the electrochemistry performance of the as-obtained Cu-N-C within 1 M KOH electrolyte. Notably, the rapid CO_2 diffusion in the flow cell achieves a significantly large CO partial current density of 131.3 mA cm^{-2} at -1.17 V (Figure 3f). Moreover, the product analysis shows that the high CO FEs above 96% could

View Article Online
DOI: 10.1039/D0TA08496D

be maintained over a wide voltage window on Cu-N-C, and the maximum CO FE of 99% was obtained at -0.67 V (Figure 3f inset). This is due to the boosted the CO_2 transfer and high alkaline condition that suppresses the H_2 production.[38] Moreover, Figure S23 showed no detectable Cu reduction/oxidation redox peaks in both H- and flow-cell reactors.

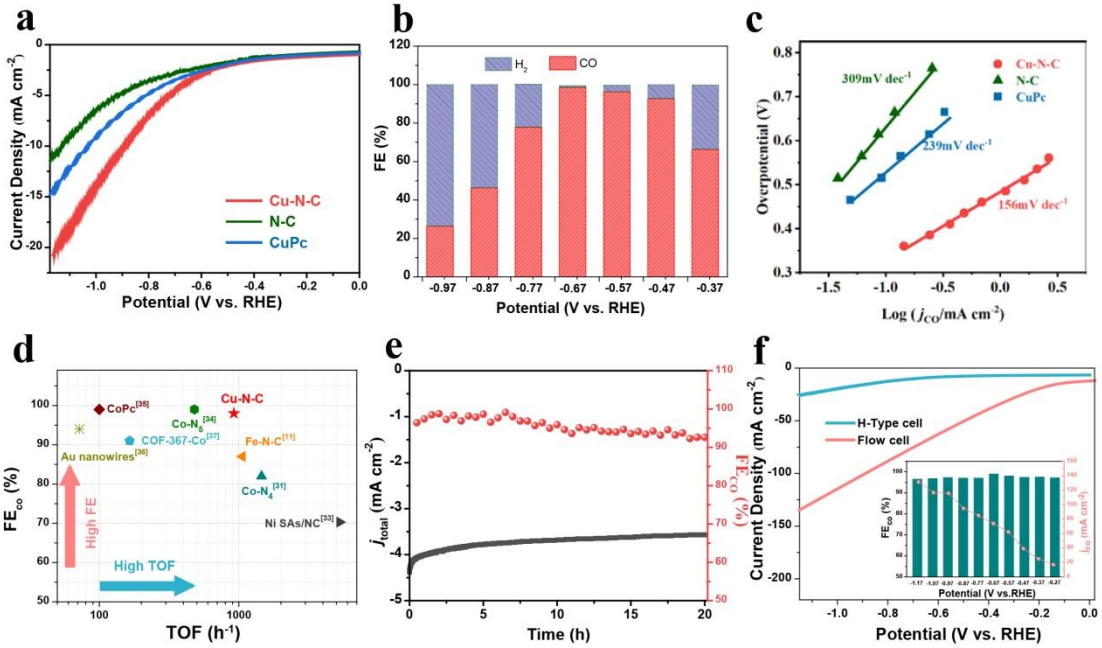

Figure 3. (a) LSV curves, (b) CO and H_2 FE of Cu-N-C; (c)Tafel plots of obtained samples; (d) FE and TOF comparison with state-of-the-art CO_2-to-CO reduction catalysts; (e) stability tests on Cu-N-C at the potentials at -0.67 V over 20 h; (f) LSV curves of Cu-N-C in the flow cell (inset is CO FE and j_{CO} for Cu-N-C in the flow cell).

Density functional theory (DFT) calculations

DFT calculations were carried out to disclose the intrinsic CO_2RR activity and the high product selectivity of Cu-N-C. For Cu-free N-C substrate, the N4-C structure and active sites, e.g., N_4-1, N_4-2, N_4-3 for C atoms and N_4-4 for N atom, for adsorption of different intermediates (*COOH for CO_2RR and *H for HER) have been constructed (Figure

View Article Online
DOI: 10.1039/D0TA08496D

S24). The lower free-energy barriers for *H formation on N4-C structure than that for *COOH formation reveal the favorable HER on N4-C structure. In contrast, for Cu-N_4, the free energy change of *H formation is uphill with 1.68 eV, implying the introduction of Cu atoms could effectively suppress the HER. The detailed discussion is provided in *Supporting Information.* Based on the EXAFS results, the Cu atoms directly coordinated with three N atoms (Cu-N_3) in the graphene plane is first constructed. The *COOH is commonly regarded as the key intermediate for CO formation.[39,40] In the free energy evaluation plot (Figure 4a), the Gibbs free energy barrier of CO_2(g)→*COOH on Cu-N_3 was calculated to be 1.0 eV, which is lower than that on Cu-N_4 (1.65 eV). However, the CO desorption on the Cu-N_3 structure is extremely difficult with an unreasonable energy barrier of 2.84 eV. The following in-depth investigation revealed that the lower energy barrier on *COOH or *CO desorption on Cu-N_3 is caused by the severe structure distortion, not originate from the intrinsic activity improvement (Figures 4b and 4c). Thus, the directly coordinated Cu-N_3 structure is excluded for further investigation. Furthermore, another possible Cu-N_3 structure with three carbon vacancies model (Cu-N_3C_3) was constructed (Figure 4d), in which the Cu atom could not be stabilized by three N atoms, but the Cu atom will be energy-favorably coordinated by one N and two C atoms (Cu-NC_2, Figure 4e). When the structure was evaluated for CO_2RR activity, the Gibbs free energy diagram is very similar to that of Cu-N_4 and displays no superior electrocatalytic activity (Figure 4f).

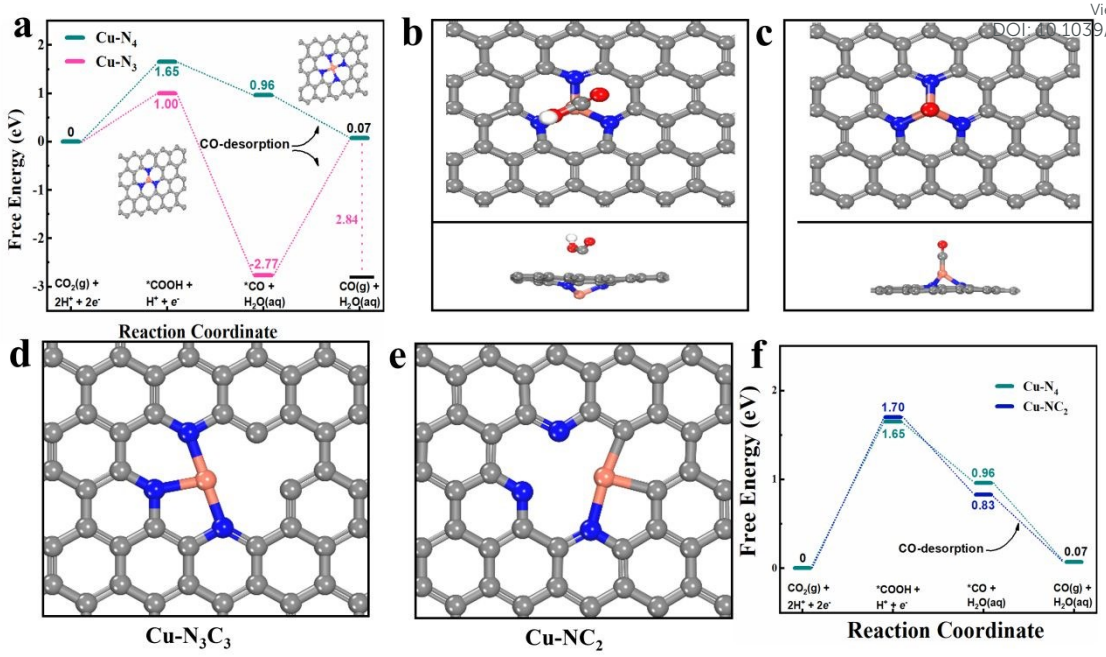

Figure 4 (a) Calculated Gibbs free energy diagrams for CO_2RR on Cu-N_4 and Cu-N_3; Optimized atomic structures for (b) *COOH and (c) *CO intermediates adsorbed on Cu sites. The simulated structure of (d) Cu-N_3C_3 and (e) Cu-NC_2; (f) Calculated Gibbs free energy evolution of CO_2RR reduction to CO on Cu-NC_2 and Cu-N_4 at an applied electrode potential (U) of 0 V.

In order to provide a plausible explanation for the experiment results, the Cu-N_3 structure within six N vacancies in a graphene plane (Cu-N_3N_3) was further constructed and investigated (Figure 5a).[41,42] This structure can stably tri-coordinate with the Cu atom with Cu-N coordination distances of 1.92, 1.93, and 2.06 Å. The Gibbs free energy diagram disclosed that the energy barrier of $CO_2(g)\rightarrow$*COOH on Cu-N_3N_3 efficiently decreases to 1.36 eV, lower than that of Cu-N_4 (1.65 eV, Figure 5b). The formation energy of Cu-N_3N_3 is predicted to be 1.87 eV that is slightly higher than that of Cu-N_4 (1.67 eV), suggesting the modeling rationality and synthesis feasibility of Cu-N_3N_3 structure. However, in the following HER calculation, the H could not be adsorbed on

View Article Online
DOI: 10.1039/D0TA08496D

the Cu center and will simultaneously transfer to the adjacent N site with a Cu-N distance of 2.44 Å (Figure 5c). This phenomenon strongly suggested that the three uncoordinated N sites will be easily saturated by protons in the electrolyte. Therefore, the proton-saturated CuN_6 model (HS-CuN_6) was further built and evaluated (Figure 5d). Impressively, the energy barrier of CO_2(g)→*COOH significantly reduced to 0.65 eV (Figure 5e), which is even lower than the most advantageous free-energy of Ni-N_4 (0.84 eV).[24] Interestingly, a unique hydrogen-bond promoted CO_2RR activity was disclosed after we constructed the *COOH adsorbed structure. As shown in Figure 5f, the adsorbed *COOH on the Cu atom could form an obvious hydrogen-bond interaction with an O-H distance of 1.74 Å that will significantly strengthen the *COOH adsorption and lower the CO_2(g)→*COOH energy barrier. After the first proton-coupled electron transfer process, the hydrogen-bond disappears, and as such the *CO could be easily released to boost the CO production. The corresponding reaction route for CO_2RR was displayed in Figure S25. Moreover, even within the HS-CuN_6 system, the energy barrier for HER was calculated to be 0.83 eV, which is higher than that of CO_2RR (0.65 eV), demonstrating the high selectivity toward CO_2RR (Figure S26). In addition, Figure S27 depicted that the calculated adsorption energy of CO_2 is -0.21 eV on HS-CuN_6, higher than that of Cu-N_4 (-0.16 eV) and Cu-N_3N_3 (-0.18 eV), suggesting the proton-saturated model facilitate the initial CO_2 adsorption on the catalyst surface. Thus, the key roles of H-bond in Cu-N_3N_3 can be attributed to: 1). the boosted chemisorption of CO_2 by the H bonding; 2). the enhanced adsorption of *COOH intermediate; 3). the facilitated proton transfer from water. These merits eventually explained the high selectivity for

View Article Online
DOI: 10.1039/D0TA08496D

CO_2RR over the HER.

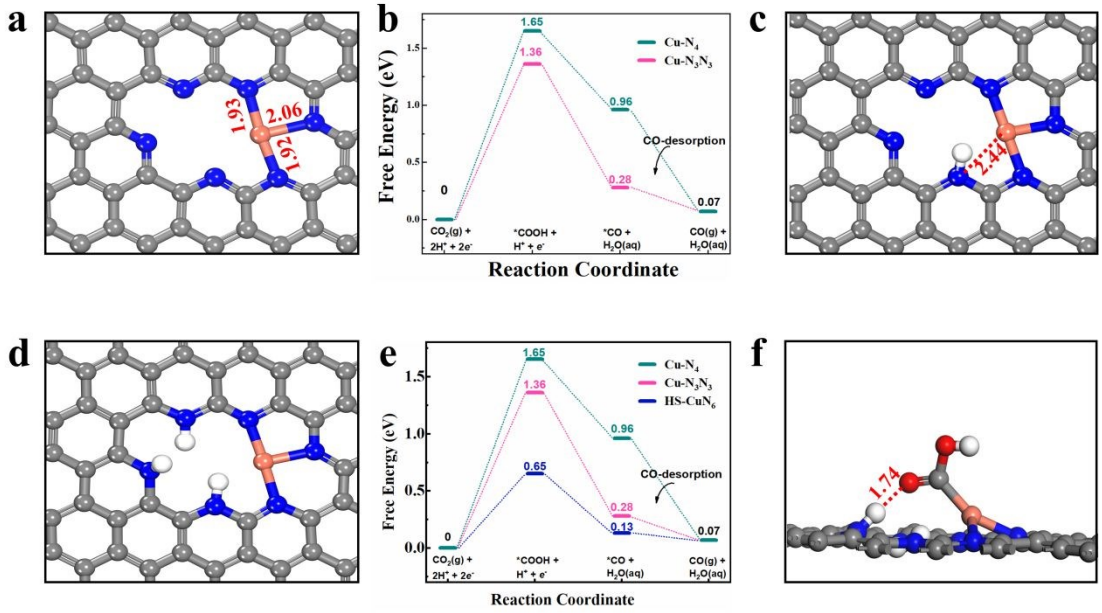

Figure 5 (a) Atomic structure of Cu-N_3N_3; (b) Calculated Gibbs free energy evolution of CO_2RR on Cu-N_4 and Cu-N_3N_3 at an applied electrode potential (U) of 0 V; The structure of (c) Cu-N_3N_3 active sites with the H simultaneously transfer to the adjacent N site, and (d) three H-saturated N sites of HS-CuN_6; (e) Calculated Gibbs free energy evolution of CO_2RR on Cu-N_4, Cu-N_3N_3, and HS-CuN_6 at an applied electrode potential (U) of 0 V; (f) The optimized atomic structures of Cu-N-C with an *COOH intermediate adsorbed on Cu sites.

CONCLUSION

In summary, we have successfully synthesized a well-defined and atomically dispersed Cu electrocatalyst for efficient and selective CO production. The catalytically active center is identified by systematical structure investigations and DFT calculations. The Cu-N-C delivers a high CO FE of 98% at -0.67 V (vs. the RHE). The durability of Cu-N-C is verified by the steady consecutive CO_2RR over 20 h. In flow cell configuration, both high CO FE of 99% at -0.67 V and large partial density of 131.3 mA cm^{-2} at -1.17 V can be reached. The mechanistic study reveals a novel proton-

View Article Online
DOI: 10.1039/D0TA08496D

saturated Cu-N_6 structure, which can form an extra hydrogen-bond between the saturated H and adsorbed *COOH, is responsible for the enhanced CO_2RR activity and selectivity. This work provides in-depth insights into the mechanism of CO production on Cu-N-C structures and can inspire future rational design of CO_2RR catalysts with high efficiency and selectivity.

ASSOCIATED CONTENTS

Supporting Information: The Supporting Information is available free of charge on the ACS Publications website at DOI: Supporting Information section describes experiment details and more supplementary analysis. Figures S1-S27 address additional characterization of interest and details regarding the catalytic tests, including SEM images, XRD patterns, XPS data, Raman measurement, CO_2 electroreduction activity, and ^{13}C isotope labeling experiments. Table S1-S4 provide detailed physical properties.

AUTHOR INFORMATION

Corresponding Author

*Email: jwang7@ncu.edu.cn (J.W)

*Email: shuguang.deng@asu.edu (SG.D)

Notes

The authors declare no competing financial interest.

View Article Online
DOI: 10.1039/D0TA08496D

ACKNOWLEDGMENTS

This research work was supported by the National Natural Science Foundation of China (No. 21908090) and the Natural Science Foundation of Jiangxi Province (No. 20192ACB21015). The authors would like to thank the helpful discussions and suggestions from Prof. Troels Skrydstrup and Dr. Xinming Hu at Aarhus University, Denmark and Dr. Yuxing Huang and Dr. Xin Zhuo at Nanchang University, P.R China.

REFERENCES

1 Q. Wang, J. Luo, Z. Zhong and A. Borgna, *Energy Environ. Sci.*, 2011, **4**, 42–55.

2 E. S. Sanz-Pérez, C. R. Murdock, S. A. Didas and C. W. Jones, *Chem. Rev.*, 2016, **116**, 11840–11876.

3 R. S. H. Khoo, H.-K. Luo, P. Braunstein and T. S. A. Hor, *J. Mol. Eng. Mater.*, 2015, **03**, 1540007.

4 C. Long, X. Li, J. Guo, Y. Shi, S. Liu and Z. Tang, *Small Methods*, 2018, **3**, 1800369.

5 R. Francke, B. Schille and M. Roemelt, *Chem. Rev.*, 2018, **118**, 4631–4701.

6 D. U. Nielsen, X. M. Hu, K. Daasbjerg and T. Skrydstrup, *Nat. Catal.*, 2018, **1**,

View Article Online
DOI: 10.1039/D0TA08496D

244–254.

7 X. Wang, Z. Chen, X. Zhao, T. Yao, W. Chen, R. You, C. Zhao, G. Wu, J. Wang, W. Huang, J. Yang, X. Hong, S. Wei, Y. Wu and Y. Li, *Angew. Chemie - Int. Ed.*, 2018, **57**, 1944–1948.

8 W. Ren, X. Tan, W. Yang, C. Jia, S. Xu, K. Wang, S. C. Smith and C. Zhao, *Angew. Chemie - Int. Ed.*, 2019, **58**, 6972–6976.

9 A. S. Varela, N. Ranjbar Sahraie, J. Steinberg, W. Ju, H.-S. Oh and P. Strasser, *Angew. Chemie*, 2015, **127**, 10908–10912.

10 G. A. Ferrero, K. Preuss, A. Marinovic, A. B. Jorge, N. Mansor, D. J. L. Brett, A. B. Fuertes, M. Sevilla and M. M. Titirici, *ACS Nano*, 2016, 10, 5922–5932.

11 F. Pan, W. Deng, C. Justiniano and Y. Li, *Appl. Catal. B Environ.*, 2018, **226**, 463–472.

12 X. M. Hu, H. H. Hval, E. T. Bjerglund, K. J. Dalgaard, M. R. Madsen, M. M. Pohl, E. Welter, P. Lamagni, K. B. Buhl, M. Bremholm, M. Beller, S. U. Pedersen, T. Skrydstrup and K. Daasbjerg, *ACS Catal.*, 2018, **8**, 6255–6264.

13 A. S. Varela, M. Kroschel, T. Reier and P. Strasser, *Catal. Today*, 2016, **260**, 8–13.

14 T. N. Huan, N. Ranjbar, G. Rousse, M. Sougrati, A. Zitolo, V. Mougel, F. Jaouen and M. Fontecave, *ACS Catal.*, 2017, **7**, 1520–1525.

15 Y. Ye, F. Cai, H. Li, H. Wu, G. Wang, Y. Li, S. Miao, S. Xie, R. Si, J. Wang and X. Bao, *Nano Energy*, 2017, **38**, 281–289.

16 H. Bin Yang, S. F. Hung, S. Liu, K. Yuan, S. Miao, L. Zhang, X. Huang, H. Y.

Wang, W. Cai, R. Chen, J. Gao, X. Yang, W. Chen, Y. Huang, H. M. Chen, C. M. Li, T. Zhang and B. Liu, *Nat. Energy*, 2018, **3**, 140–147.

17 T. Möller, W. Ju, A. Bagger, X. Wang, F. Luo, T. Ngo Thanh, A. S. Varela, J. Rossmeisl and P. Strasser, *Energy Environ. Sci.*, 2019, **12**, 640–647.

18 C. Zhao, Y. Wang, Z. Li, W. Chen, Q. Xu, D. He, D. Xi, Q. Zhang, T. Yuan, Y. Qu, J. Yang, F. Zhou, Z. Yang, X. Wang, J. Wang, J. Luo, Y. Li, H. Duan, Y. Wu and Y. Li, *Joule*, 2019, **3**, 584–594.

19 H. Yang, Y. Wu, G. Li, Q. Lin, Q. Hu, Q. Zhang, J. Liu and C. He, *J. Am. Chem. Soc.*, 2019, **141**, 12717–12723.

20 D. Karapinar, N. T. Huan, N. Ranjbar Sahraie, J. Li, D. Wakerley, N. Touati, S. Zanna, D. Taverna, L. H. Galvão Tizei, A. Zitolo, F. Jaouen, V. Mougel and M. Fontecave, *Angew. Chemie - Int. Ed.*, 2019, **58**, 15098–15103.

21 F. Yang, X. Mao, M. Ma, C. Jiang, P. Zhang, J. Wang, Q. Deng, Z. Zeng and S. Deng, *Carbon N. Y.*, 2020, **168**, 528–535.

22 X. Han, X. Ling, Y. Wang, T. Ma, C. Zhong, W. Hu and Y. Deng, *Angew. Chemie - Int. Ed.*, 2019, **58**, 5359–5364.

23 A. C. Ferrari, *Solid State Commun.*, 2007, **143**, 47–57.

24 C. E. Tornow, M. R. Thorson, S. Ma, A. A. Gewirth and P. J. A. Kenis, *J. Am. Chem. Soc.*, 2012, **134**, 19520–19523.

25 N. R. Sahraie, U. I. Kramm, J. Steinberg, Y. Zhang, A. Thomas, T. Reier, J. P. Paraknowitsch and P. Strasser, *Nat. Commun.*, 2015, **6**, 1–9.

26 Q. Lai, L. Zheng, Y. Liang, J. He, J. Zhao and J. Chen, *ACS Catal.*, 2017, **7**,

View Article Online
DOI: 10.1039/D0TA08496D

1655–1663.

27 D. Karapinar, A. Zitolo, T. N. Huan, S. Zanna, D. Taverna, L. H. Galvão Tizei, D. Giaume, P. Marcus, V. Mougel and M. Fontecave, *ChemSusChem*, 2020, **13**, 173–179.

28 Y. Qu, Z. Li, W. Chen, Y. Lin, T. Yuan, Z. Yang, C. Zhao, J. Wang, C. Zhao, X. Wang, F. Zhou, Z. Zhuang, Y. Wu and Y. Li, *Nat. Catal.*, 2018, **1**, 781–786.

29 T. Zhang, D. Zhang, X. Han, T. Dong, X. Guo, C. Song, R. Si, W. Liu, Y. Liu and Z. Zhao, *J. Am. Chem. Soc.*, 2018, **140**, 16936–16940.

30 C. Yan, H. Li, Y. Ye, H. Wu, F. Cai, R. Si, J. Xiao, S. Miao, S. Xie, F. Yang, Y. Li, G. Wang and X. Bao, *Energy Environ. Sci.*, 2018, **11**, 1204–1210.

31 Z. Geng, Y. Cao, W. Chen, X. Kong, Y. Liu, T. Yao and Y. Lin, *Appl. Catal. B Environ.*, 2019, **240**, 234–240.

32 F. Pan, H. Zhang, K. Liu, D. Cullen, K. More, M. Wang, Z. Feng, G. Wang, G. Wu and Y. Li, *ACS Catal.*, 2018, **8**, 3116–3122.

33 C. Zhao, X. Dai, T. Yao, W. Chen, X. Wang, J. Wang, J. Yang, S. Wei, Y. Wu and Y. Li, *J. Am. Chem. Soc.*, 2017, **139**, 8078–8081.

34 Y. Pan, R. Lin, Y. Chen, S. Liu, W. Zhu, X. Cao, W. Chen, K. Wu, W.-C. Cheong, Y. Wang, L. Zheng, J. Luo, Y. Lin, Y. Liu, C. Liu, J. Li, Q. Lu, X. Chen, D. Wang, Q. Peng, C. Chen and Y. Li, *J. Am. Chem. Soc.*, 2018, **140**, 4218–4221.

35 Z. Zhang, J. Xiao, X. J. Chen, S. Yu, L. Yu, R. Si, Y. Wang, S. Wang, X. Meng, Y. Wang, Z. Q. Tian and D. Deng, *Angew. Chemie - Int. Ed.*, 2018, **57**, 16339–16342.

View Article Online
DOI: 10.1039/D0TA08496D

36 W. Zhu, Y. J. Zhang, H. Zhang, H. Lv, Q. Li, R. Michalsky, A. A. Peterson and S. Sun, *J. Am. Chem. Soc.*, 2014, **136**, 16132–16135.

37 J. Shen, R. Kortlever, R. Kas, Y. Y. Birdja, O. Diaz-Morales, Y. Kwon, I. Ledezma-Yanez, K. J. P. Schouten, G. Mul and M. T. M. Koper, *Nat. Commun.*, 2015, **6**, 1–8.

38 G. L. De Gregorio, T. Burdyny, A. Loiudice, P. Iyengar, W. A. Smith and R. Buonsanti, *ACS Catal.*, 2020, **10**, 4854–4862.

39 Y. Y. Birdja, E. Pérez-Gallent, M. C. Figueiredo, A. J. Göttle, F. Calle-Vallejo and M. T. M. Koper, *Nat. Energy*, 2019, **4**, 732–745.

40 Z. Geng, X. Kong, W. Chen, H. Su, Y. Liu, F. Cai, G. Wang and J. Zeng, *Angew. Chemie - Int. Ed.*, 2018, **57**, 6054–6059.

41 J. Wang, Z. Huang, W. Liu, C. Chang, H. Tang, Z. Li, W. Chen, C. Jia, T. Yao, S. Wei, Y. Wu and Y. Li, *J. Am. Chem. Soc.*, 2017, 139, 17281–17284.

42 W. Ye, S. Chen, Y. Lin, L. Yang, S. Chen, X. Zheng, Z. Qi, C. Wang, R. Long, M. Chen, J. Zhu, P. Gao, L. Song, J. Jiang and Y. Xiong, *Chem*, 2019, **5**, 2865–2878.